

Lawrence Berkeley National Laboratory

LBL Publications

Title

Large Magnetic Gap in a Designer Ferromagnet—Topological Insulator—Ferromagnet Heterostructure

Permalink

<https://escholarship.org/uc/item/52d904ks>

Journal

Advanced Materials, 34(21)

ISSN

0935-9648

Authors

Li, Qile

Trang, Chi Xuan

Wu, Weikang

et al.

Publication Date

2022-05-01

DOI

10.1002/adma.202107520

Peer reviewed

Large Magnetic Gap in a Designer Ferromagnet–Topological Insulator–Ferromagnet Heterostructure

Qile Li,^{*} Chi Xuan Trang, Weikang Wu, Jinwoong Hwang, David Cortie, Nikhil Medhekar, Sung-Kwan Mo, Shengyuan A. Yang, and Mark T. Edmonds^{*}

Combining magnetism and nontrivial band topology gives rise to quantum anomalous Hall (QAH) insulators and exotic quantum phases such as the QAH effect where current flows without dissipation along quantized edge states. Inducing magnetic order in topological insulators via proximity to a magnetic material offers a promising pathway toward achieving the QAH effect at a high temperature for lossless transport applications. One promising architecture involves a sandwich structure comprising two single-septuple layers (1SL) of MnBi_2Te_4 (a 2D ferromagnetic insulator) with ultrathin few quintuple layer (QL) Bi_2Te_3 in the middle, and it is predicted to yield a robust QAH insulator phase with a large bandgap greater than 50 meV. Here, the growth of a 1SL MnBi_2Te_4 /4QL Bi_2Te_3 /1SL MnBi_2Te_4 heterostructure via molecular beam epitaxy is demonstrated and the electronic structure probed using angle-resolved photoelectron spectroscopy. Strong hexagonally warped massive Dirac fermions and a bandgap of 75 ± 15 meV are observed. The magnetic origin of the gap is confirmed by the observation of the exchange-Rashba effect, as well as the vanishing bandgap above the Curie temperature, in agreement with density functional theory calculations. These findings provide insights into magnetic proximity effects in topological insulators and reveal a promising platform for realizing the QAH effect at elevated temperatures.


1. Introduction

3D topological insulators (TIs) are materials with non-trivial band topology that are distinct from regular band insulators. Due to strong spin–orbit coupling, band inversion, and bulk boundary correspondence, the surfaces of 3D TIs host spin polarized massless Dirac cones that are robust against time reversal symmetric (TRS) perturbations.^[1–3] By introducing long-range magnetic order in the 3D TI, TRS can be broken, which manifests as a gap opening in the Dirac cones due to exchange interaction and gives rise to novel phases such as the quantum anomalous Hall (QAH) insulator and axion insulator.^[4–6] A QAH insulator possesses chiral edge states within the bandgap, and when the chemical potential is tuned into the magnetic gap a quantized Hall conductance and almost zero longitudinal resistance is observed known as the QAH effect.^[7,8] Characterized by dissipationless charge transport and perfect spin

Q. Li, C. X. Trang, M. T. Edmonds
School of Physics and Astronomy
Monash University
Clayton, VIC 3800, Australia
E-mail: qile.li@monash.edu; mark.edmonds@monash.edu

Q. Li, C. X. Trang, N. Medhekar, M. T. Edmonds
ARC Centre for Future Low Energy Electronics Technologies
Monash University
Clayton, VIC 3800, Australia

Q. Li, N. Medhekar
Department of Materials Science and Engineering
Monash University
Clayton, VIC 3800, Australia

 The ORCID identification number(s) for the author(s) of this article can be found under <https://doi.org/10.1002/adma.202107520>.

© 2022 The Authors. Advanced Materials published by Wiley-VCH GmbH. This is an open access article under the terms of the Creative Commons Attribution License, which permits use, distribution and reproduction in any medium, provided the original work is properly cited.

DOI: 10.1002/adma.202107520

W. Wu, S. A. Yang
Research Laboratory for Quantum Materials
Singapore University of Technology and Design
Singapore 487372, Singapore

W. Wu
Division of Physics and Applied Physics
School of Physical and Mathematical Sciences
Nanyang Technological University
Singapore 637371, Singapore

J. Hwang, S.-K. Mo
Advanced Light Source
Lawrence Berkeley National Laboratory
Berkeley, CA 94720, USA

D. Cortie
Australian Nuclear Science and Technology Organization
Lucas Heights, NSW 2234, Australia

D. Cortie
Institute for Superconductivity and Electronic Materials
University of Wollongong
Wollongong, NSW 2522, Australia

polarization, QAH insulators have potential applications in lossless transport, spintronics, and topological quantum computing involving braiding of Majorana fermions.^[9]

To date, the QAH effect has been observed in dilute magnetically doped ultrathin TIs^[7,8] at 30 mK, and up to 1 K in modulation-doped sandwich heterostructures,^[10] and most recently in five-layer exfoliated flakes of the intrinsic magnetic topological insulator, MnBi_2Te_4 at 1.4 K.^[11] However, the temperature at which the QAH effect is observed in these systems is well below the size of the magnetic gap and the Curie temperature. This is a result of magnetic disorder^[12] and the difficulty in incorporating 3d transition metal magnetic dopants.

Rather than incorporating 3d transition metals into the crystal lattice, a more advantageous strategy may be to place two ferromagnetic materials on the top and bottom surfaces of a 3D TI.^[13] This will break TRS for topological surface states (TSS) at the two surfaces via magnetic proximity, thereby opening an exchange gap and giving rise to a QAH insulator or axion insulator phase^[14,15] (depending on the thickness of the TI layer). However, inducing sufficient magnetic order to open a sizeable exchange gap via proximity effects is challenging due to the undesired influence of the abrupt interface potential as a consequence of lattice mismatch between the magnetic material and TI.^[16] To date, the only demonstration of QAH effect in a ferromagnetic insulator (FMI)–topological insulator (TI)–ferromagnetic insulator (FMI) heterostructure has been in $(\text{Zn}_{1-x}\text{Cr}_x)\text{Te}$ – $(\text{Bi}_{1-y}\text{Sb}_y)_2\text{Te}_3$ – $(\text{Zn}_{1-x}\text{Cr}_x)\text{Te}$, and did not yield an improvement in the temperature at which QAH effect was observed in comparison to dilute magnetically doped 3D TIs.^[17]

Minimizing the interface potential when inducing magnetic order via proximity necessitates the use of FMI such as CrI_3 ,^[18] CrGeTe_3 ,^[19] and single-septuple-layer MnBi_2Te_4 ^[20] that possess similar chemical and structural compositions to 3D topological insulators. A single-septuple layer of the intrinsic magnetic topological insulator MnBi_2Te_4 is particularly promising.^[21] Single-septuple-layer MnBi_2Te_4 possesses a bandgap exceeding 780 meV,^[22] and has long-range ferromagnetic order (arising from the Mn^{2+} ions that contribute a $5\mu_B$ magnetic moment, with the moments coupled ferromagnetically within each layer) and a predicted Curie temperature between 12–20 K.^[20,21] Importantly, it is structurally similar to the well-known 3D TI Bi_2Te_3 (BT), with the in-plane lattice constant of MnBi_2Te_4 (0.433 nm)^[21] almost identical to Bi_2Te_3 (0.438 nm).^[23] Furthermore, single layer MnBi_2Te_4 and Bi_2Te_3 can be grown with molecular beam epitaxy (MBE)^[22,23] allowing the possibility to engineer new ferromagnet/TI heterostructures. This offers simplicity and control far greater than using 2D exfoliation and heterostructure stacking of different van der Waals (vdW) materials such as Bi_2Te_3 and CrI_3 .^[24]

The near-identical crystal and atomic structures of MnBi_2Te_4 and Bi_2Te_3 means that instead of an abrupt interface potential there is a magnetic extension of the Bi_2Te_3 TSS into the MnBi_2Te_4 magnetic layer as depicted in **Figure 1a**. This strong interaction of the TI surface states with the Mn^{2+} ions induce a significant exchange splitting in the TSS of the topological insulator thin film and opens a large gap. This type of magnetic extension was first demonstrated on the top surface of a FMI/TI heterostructure comprising 15 quintuple-layer (QL) Bi_2Se_3 with a single layer of MnBi_2Se_4 on the top surface, which

yielded a bandgap ≈ 100 meV.^[25] However, with only the top TSS gapped and a 15 QL TI layer, the bottom surface would remain gapless and unlikely to yield the QAH effect. A new theoretical proposal showed that if both the top and bottom TSS of an ultrathin Bi_2Te_3 film are gapped by MnBi_2Te_4 (MBT) layers and the inverted band structure is preserved, chiral spin-polarized edge states and a wide-bandgap QAH insulator can be formed.^[26] In this case, depending on the thickness of the Bi_2Te_3 in the heterostructure the bandgap is predicted to be between 38 meV for 1QL Bi_2Te_3 and between 56–61 meV for 2 to 5 QL Bi_2Te_3 .^[26]

In this work, we demonstrate the epitaxial growth of such a heterostructure which comprises 4 QL Bi_2Te_3 sandwiched between two single septuple-layers (SL) of MnBi_2Te_4 ($[\text{MnBi}_2\text{Te}_4]_{\text{SL}}$ – $[\text{Bi}_2\text{Te}_3]_{4\text{QL}}$ – $[\text{MnBi}_2\text{Te}_4]_{\text{SL}}$). For simplicity, for the remainder of the paper, we will refer to this structure as MBT/BT/MBT. We then utilize angle-resolved photoelectron spectroscopy (ARPES) at 8 K, which is below the Curie temperature, $T_c = 12$ –20 K of 1 SL MnBi_2Te_4 to measure the electronic band structure and size of the induced exchange gap. We observed strong band anisotropy and large hexagonal warping of the massive Dirac fermion, with a gap of 75 ± 15 meV and magnetization measurements showing a Curie temperature of ≈ 20 –30 K for this heterostructure, making it a promising avenue towards measuring the QAH effect at elevated temperatures.

2. Results and Discussion

High-quality ultrathin MnBi_2Te_4 and Bi_2Te_3 films and the MBT/BT/MBT heterostructure were grown using MBE on Si (111) 7×7 substrates. These growths followed established growth procedures that allow for MnBi_2Te_4 and Bi_2Te_3 to be grown down to single layer thickness.^[22,23] Figure S1a,b, Supporting Information, shows the layer-by-layer growth mode of the Bi_2Te_3 at the optimal growth temperature of 230 °C demonstrating we can precisely control the film thickness. The oscillation period of 1QL/140s allows us to grow 4 QL Bi_2Te_3 in a layer-by-layer manner. After the desired thickness of Bi_2Te_3 is reached, we then deposit a bilayer of MnTe in order to spontaneously form a septuple layer (SL) of MnBi_2Te_4 . We determine the bilayer of MnTe using the deposition rates of Mn, and the intensity of the reflection high-energy electron diffraction (RHEED) pattern during deposition. As shown in Figure S1c–e, Supporting Information, with deposition of MnTe on top of Bi_2Te_3 , the diffraction streak intensity goes up and reaches a maximum (Figure S1d, Supporting Information) then drops with excessive MnTe (Figure S1e, Supporting Information). This intensity maxima indicates the formation of 1 SL MnBi_2Te_4 and deposition of MnTe is stopped at this point to optimize sample quality. The high quality of the films is confirmed from RHEED patterns shown in Figure S1, Supporting Information. The sharp, bright streaks indicate that the film is of uniform thickness and high crystallinity. Further details on the growth method can be found in the Experimental Section. Figure 1b shows the crystal structure of the MBT/BT/MBT heterostructure, with the magnetic moments from Mn atoms labelled with red arrows. Angle-integrated core level photoelectron spectroscopy was taken on

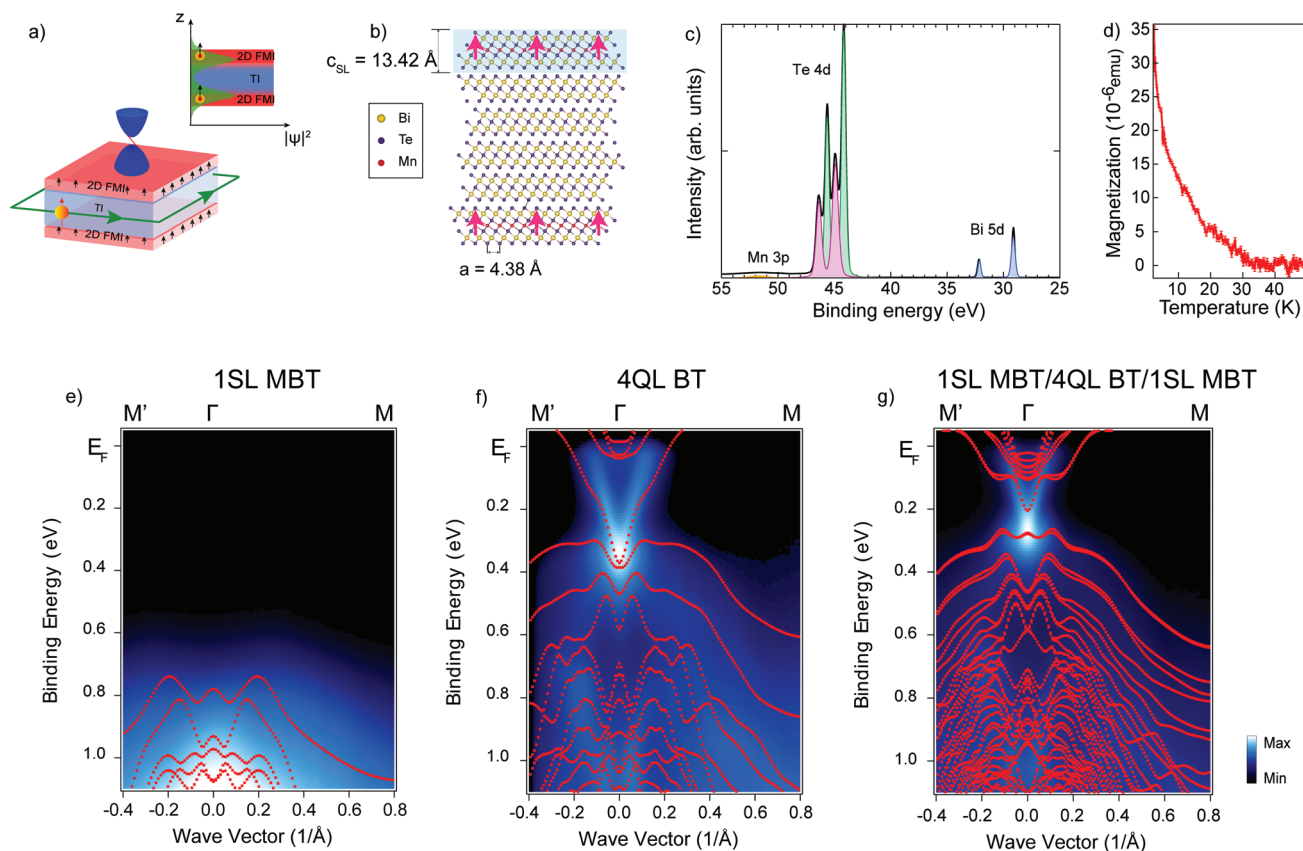


Figure 1. A designer ferromagnetic insulator–topological insulator heterostructure, 1SL MBT/4QL BT/1SL MBT. a) A schematic showing the realization of the magnetic extension effect in the ferromagnetic insulator (FMI)–topological insulator (TI) heterostructure. Top right corner: wave functions of topological surface state (TSS) (green shaded curve) penetrate into the 2D FMI because of minimal lattice mismatch at the interface, resulting in a QAH insulator with chiral edge modes. b) Crystal structure of 4 quintuple layer (QL) Bi_2Te_3 (BT) sandwiched between two 1 septuple layers (SL) MnBi_2Te_4 (MBT) with the lattice constants labelled, magnetic moments on Mn^{2+} are marked by red arrows. The shadowed block indicates 1SL MnBi_2Te_4 . c) Angle-integrated core level photoelectron spectroscopy measurement taken on the MBT/BT/MBT heterostructure at $h\nu = 100$ eV, showing the characteristic Mn 3p, Bi 5d, and Te 4d peaks. d) Temperature-dependent magnetization of the 1SL MBT/4QL BT/1SL MBT heterostructure taken with 2T magnetic field, demonstrating a Curie temperature of ≈ 20 –30 K. e–g) ARPES spectra overlaid with DFT calculations along the Γ –M direction for 1SL MnBi_2Te_4 at 13.5 K, 4QL Bi_2Te_3 at 15 K, and 1SL MBT/4QL BT/1SL MBT at 8 K respectively.

the MBT/BT/MBT heterostructure at $h\nu = 100$ eV shown in Figure 1c, and shows the expected Mn 3p, Bi 5d, and Te 4d components. However, two distinct Te 4d spin-split components separated by 0.7 eV are observed (represented with green and purple shading). The peak positions of the two Te 4d components are consistent with two chemical binding environments, one from 1 SL MnBi_2Te_4 and another from the underlying 4QL Bi_2Te_3 , as these binding energy positions are consistent with core level spectra taken independently on a 1 SL MnBi_2Te_4 film and a 4 QL Bi_2Te_3 film as shown in Figure S2, Supporting Information. Temperature-dependent magnetization measurements (details in Experimental Section) were also performed on the MBT/BT/MBT heterostructure to determine the Curie temperature as shown in Figure 1d. Magnetic-field-dependent magnetization curves taken at different temperatures between 4 and 100 K are included in Figure S3, Supporting Information. A clear increase in the magnetization occurs at ≈ 20 –30 K, which corresponds to the Curie temperature which is in good agreement with the Curie temperature predicted for single-septuple-layer MnBi_2Te_4 .^[20]

Figure 1e–g shows ARPES spectra taken on 1SL MnBi_2Te_4 , 4QL Bi_2Te_3 , and the MBT/BT/MBT heterostructure, respectively. Each spectrum is overlaid with the corresponding density functional theory (DFT)-calculated band structure. For 1SL MBT, only a M-shaped valence band is present below the Fermi level indicating a bandgap greater than 780 meV.^[22] For 4QL BT, the n-type doping and band dispersion are consistent with previous reports^[23] where the Dirac cone with Fermi velocity along ΓM , $v_F = 4.1 \pm 0.5 \times 10^5$ m s^{-1} is buried within the valence band and appears gapless within our experimental resolution, which is consistent with DFT that predicts 4 QL BT is gapless.^[27] Additional high-resolution spectra, and Fermi surface map along with overlaid DFT data can be found in Figure S4, Supporting Information. In the MBT/BT/MBT heterostructure, the band structure away from the Fermi energy (>1 eV) is remarkably similar to that of 4QL BT (see Figure S5, Supporting Information, for the full valence band) while the bands near the Dirac region are noticeably different. As shown in the DFT-calculated bands in Figure 1g, unlike in BT, the Dirac cone on the surface of the heterostructure is elevated above the M-shaped valence

band, and the Fermi velocity of the Dirac electron band away from the Dirac region along ΓM increases to $v_F = 5.0 \pm 0.5 \times 10^5 \text{ m s}^{-1}$. It is worth noting that the lower bound of the v_F in MBT/BT/MBT ($4.5 \times 10^5 \text{ m s}^{-1}$) is nearly the same as the higher bound of the v_F of Bi_2Te_3 ($4.6 \times 10^5 \text{ m s}^{-1}$) and comparable to the Fermi velocity of 5 SL MnBi_2Te_4 ($5.0 \times 10^5 \text{ m s}^{-1}$).^[22] We also investigate the effect of MnTe on the band structure, and have grown and measured a 4QL BT/MBT sample with lower MnTe concentration which has been assembled along with the high-resolution scans of 4QL BT and MBT/BT/MBT in Figure S6a–c, Supporting Information. Momentum distribution curve (MDC) analysis to these scans yields a Dirac electron band for the lower concentration of MnTe which is similar to the MBT/BT/MBT sample (i.e., $\approx 5.0 \pm 0.5 \times 10^5 \text{ m s}^{-1}$), yet the sample doping remains at a level with the BT sample. When a complete 1SL MnBi_2Te_4 forms the doping level is shifted by 80 meV. Such a doping level shift is due to intrinsic p-doping of Mn^{2+} and is consistent with our analysis of the Bi 5d core level in Figure S6d, Supporting Information, which also shows a shift of $90 \pm 15 \text{ meV}$. This indicates that the major role of the Mn^{2+} ions is to modify the crystal potential and produce an effective magnetic field in the out-of-plane direction, with negligible p–d hybridization near the Fermi level. DFT-calculated orbital projected band structures in Figure S7, Supporting Information, show that the bands in the MBT/BT/MBT heterostructure near the Dirac region are comprised of p-orbitals from Bi and Te atoms, with the Mn *d*-bands lying at a much higher binding energy.

To confirm the prediction of the QAH phase in this heterostructure, we have performed DFT calculations to obtain the Chern number and the anomalous Hall conductivity (AHC). Figure 2a shows the band structure near the Fermi level calculated with spin–orbit coupling (SOC) along the ΓK and ΓM directions with the gapped region highlighted in blue. We then calculate the AHC in Figure 2b in an energy window of $\pm 0.2 \text{ eV}$. In the 59 meV gap region (blue highlighted region) between -0.029 and 0.03 eV the conductance is quantized at $-e^2/h$. This quantized AHC indicates a non-zero Chern number of -1 and corresponds to the entire 59 meV bandgap region.

Now that we have confirmed that this sandwich heterostructure is predicted to be a QAH insulator, we turn our attention to the Dirac region of the MBT/BT/MBT heterostructure to investigate the magnetic coupling of the TI surface state, and whether a gap is opened. Figure 3a shows the raw ARPES spectra of the MBT/BT/MBT thin film taken at $h\nu = 40 \text{ eV}$. Overlaid on Figure 3a are the band dispersions extracted from energy distribution curve (EDC) analysis (red circles) and MDC analysis (yellow and green circles) discussed below. Whilst there is some spectral weight near Γ in the Dirac point region that is due to Te-orbital-related matrix elements effects (more prominent between $h\nu = 47\text{--}60 \text{ eV}$, see Figure S8, Supporting Information), the system appears to be gapped. To determine the bandgap accurately, we analyze the EDC around the Γ point. Figure 3b shows an EDC curve extracted at the Γ point in Figure 3a. There are five distinct peak features, two are located just below the Fermi level and correspond to the bulk conduction bands (BCB, labelled in red). The third and fourth peaks occur in the Dirac point regime at 0.21 and 0.28 eV (labelled in blue) while the fifth peak is a broad feature attributed to the bulk valence band $\approx 0.40 \text{ eV}$ (labelled in green). We attribute the two peaks at 0.21 and 0.28 eV to the Dirac electron band and hole band, respectively. The stronger peak at 0.28 eV is attributed to the hole band top due to the higher density of states in the nearly flat band near Γ which we depict schematically in the top right corner in Figure 3b. This clear peak splitting in the EDC spectra confirms there is a bandgap, and to confirm the size of the bandgap we fit the EDC profile with five individual Lorentzian line shapes. This fitting yields the bottom of the electron band to be 0.205 eV and the top of the hole band to be 0.280 eV, resulting in a bandgap of $75 \pm 15 \text{ meV}$. In Figure 3c, we present a stacking plot of the EDCs taken within the k range of $\pm 0.1 \text{ \AA}^{-1}$ around Γ , with the EDC at Γ represented as a black curve. The blue points are peak positions of Dirac bands obtained by fitting these EDCs with the same method used in Figure 3b), whilst the yellow points represent fitting of the BCB. Figure 3d plots the DFT band structure along the $\Gamma\text{--}M$ direction based on the spectral weight from atoms in the MBT layer

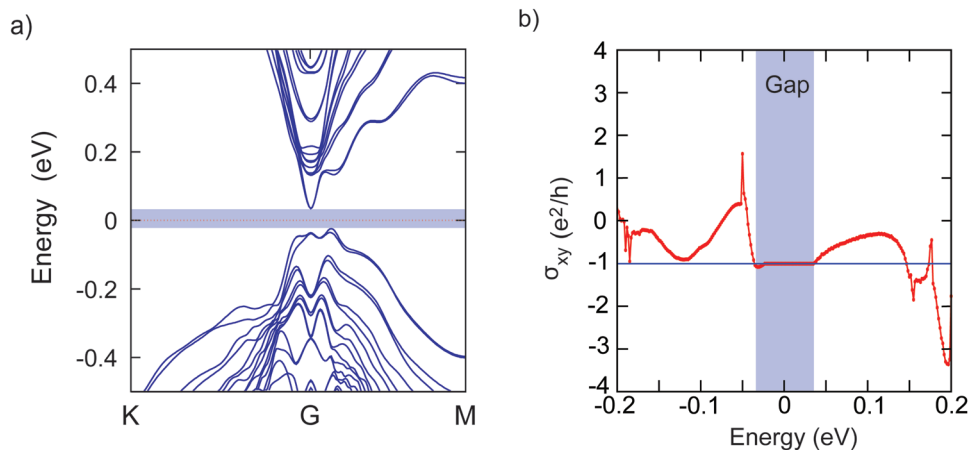


Figure 2. DFT prediction of the quantum anomalous Hall effect for the MBT/BT/MBT heterostructure. a) Band structure of the heterostructure with spin–orbit coupling and b) the anomalous Hall conductivity (AHC) calculated near the gapped region. The region where AHC reaches the quantized value of $-e^2/h$ corresponds to the 59 meV bandgap region (shaded in blue) and the same energy window has been shaded in (a) for clarity. The Chern number has been calculated to be -1 , consistent with a previous result.^[26]

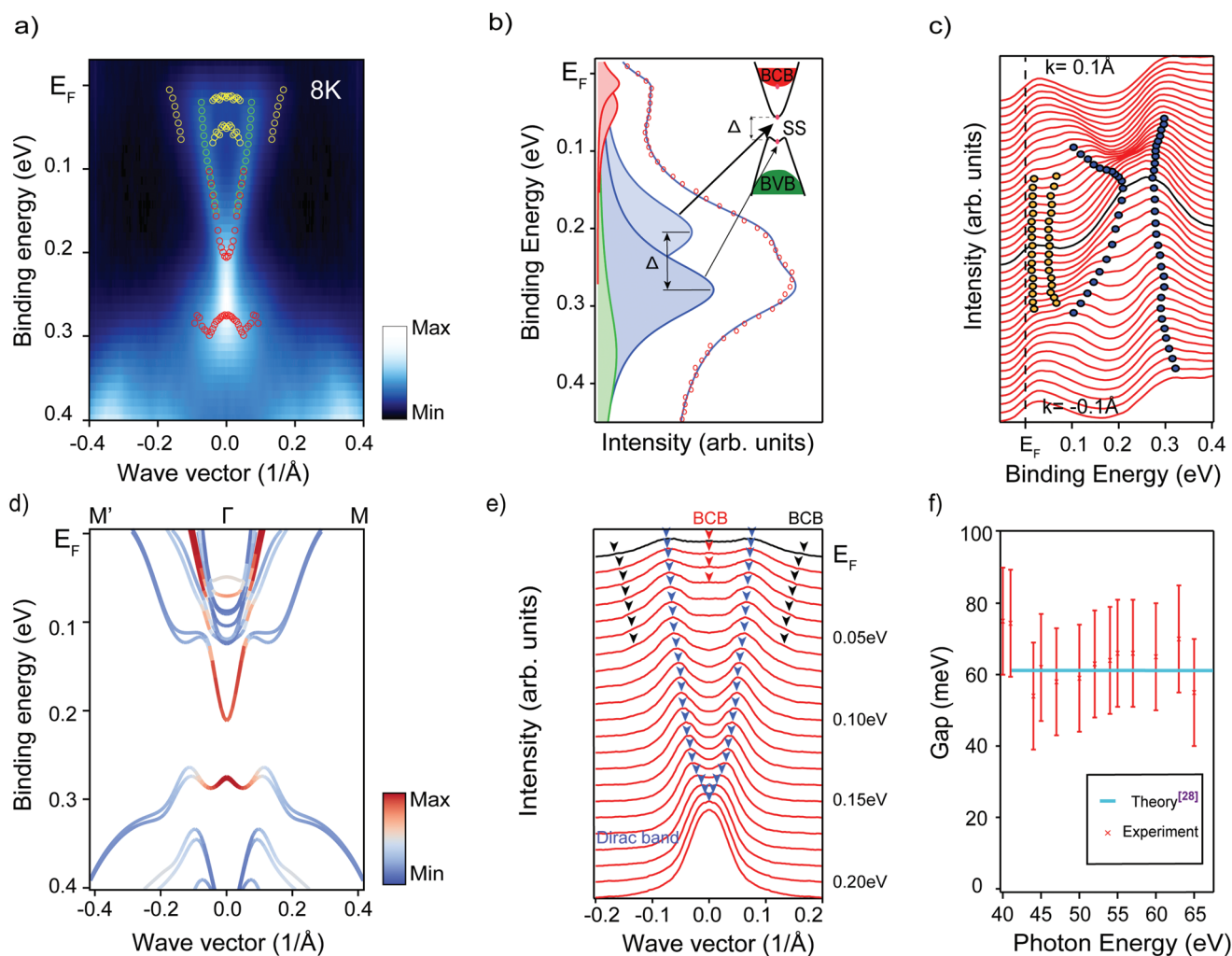


Figure 3. Bandgap analysis of MBT/BT/MBT heterostructure and its photon energy dependence. a) ARPES spectra taken on MBT/BT/MBT at $h\nu = 40$ eV at 8 K with p-polarized light. The red and yellow circles represent the dispersion of the Dirac bands and bulk conduction bands respectively, extracted from EDC analysis in (c). The green and yellow circles represent the Dirac electron band and bulk conduction band obtained from the MDC analysis in (e). b) EDC curve (red open circles) at the Γ point, with the fitted curve plotted as blue solid line. The shaded blue peaks correspond to the Dirac electron band and hole band, the red and green peaks represent the bulk conduction band (BCB) and bulk valence band (BVB), respectively. Separation of the hole band and Dirac electron band corresponds to $\Delta = 75 \pm 15$ meV. c) Stack plot of EDC curves taken within the wave vector range $\pm 0.1 \text{ \AA}^{-1}$. The EDC curve at Γ is highlighted in black and the blue points are the peak positions of the Dirac electron band and the yellow points are the positions of the bulk conduction bands. d) Surface projected DFT bands along $M'-\Gamma-M$. e) MDC stacking plot taken from 0.2 eV binding energy up to the Fermi level where the Dirac electron band is marked by the blue arrows and the bulk conduction bands with the red and black arrows. f) Bandgap obtained from EDC analysis as a function of photon energy (red markers), the DFT-predicted bandgap is plotted as a horizontal blue line.^[26] Average bandgap across all photon energies is 64 ± 15 meV.

on the top surface, with a predicted bandgap of 59 meV. In Figure 3e, we present a stacking plot of the MDCs taken from 0.2 eV up to E_F . At 0.2 eV there is only a single peak located at Γ , as we move towards the Fermi level, this peak splits into two dominant peaks that disperse linearly outwards and represent the Dirac electron band, and are marked by blue arrows. Near the Fermi level there are additional weaker components to either side of the Dirac band $\approx 0.2 \text{ \AA}^{-1}$ away from Γ marked by black arrows. Based on the dispersion and weak spectral weight, we assign these components to the bulk conduction band, as they match the DFT-predicted bulk band dispersion (blue in Figure 3d). An additional weak component is observed near Γ close to the Fermi level, which is also related to the

bulk conduction band which we label with red arrows. Overall, there is good agreement between the experimentally measured band dispersion and DFT. Photon-energy-dependent ARPES spectra between 40–65 eV at 8 K were also analyzed using the EDC peak fitting method to confirm the 2D nature of the heterostructure and that the massive Dirac gap does not change with photon energy. Figure 3f plots bandgap as a function of photon energy, and across all photon energies the fluctuation of the bandgap is within our energy resolution of ± 15 meV, which confirms the 2D nature of the bandgap. We now investigate the response of the topological electronic structure to magnetic ordering, by conducting ARPES measurements at 50 K, which is well above the measured Curie temperature. Figure S9,

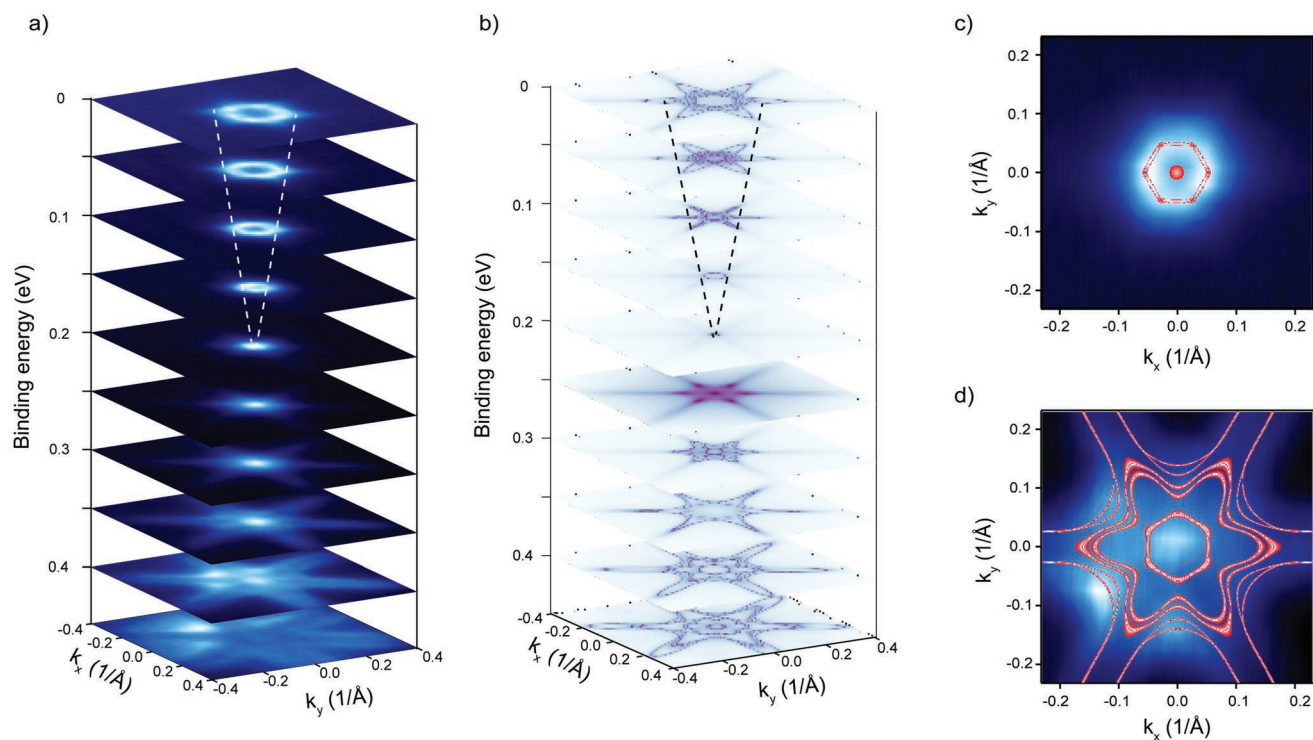


Figure 4. Strong hexagonal warping in the MBT/BT/MBT heterostructure. a) iso-energy scans taken on MBT/BT/MBT across the gap region between the Fermi level and 0.4 eV. b) DFT-calculated iso-energy scans in the same energy range showing good agreement. The dashed lines of the Dirac electron band are a guide to the eye. c,d) iso-energy cut at 0.13 eV (c) and 0.4 eV (d) binding energy overlaid with DFT-calculated contours in red. The angular intensity distribution shows threefold symmetry which agrees with the contour calculated by DFT.

Supporting Information, shows the ARPES spectrum taken at 50 K (a), and the EDC at $k_{\parallel} = 0$ (b,c). In Figure S9b, Supporting Information, the data is fit with the same peak fitting procedure used for the 8 K data. At 50 K, the pronounced shoulder observed at 8 K vanishes, and the separation between the two peak components (blue peaks in Figure S9b, Supporting Information) corresponding to the Dirac bands decreases, yielding a bandgap of $\Delta = 12$ meV, which is significantly lower than the 75 meV bandgap observed below the Curie temperature. In Figure S9c, Supporting Information, we also demonstrate that the TSS can be fit with a single peak component, which reflects that the system above the Curie temperature is a gapless topological insulator. This clear emergence of a magnetization-induced gap with decreasing temperature provides a definitive signature for a temperature-dependent topological phase transition from a large band QAH insulator phase to a paramagnetic gapless topological insulator phase.

In Figures 4 and 5, we now turn to the anisotropy and band warping in the MBT/BT/MBT heterostructure by fitting to a gapped Dirac band model, which self-consistently reassures the bandgap value determined from the EDC analysis described above. In Figures 4a,b, we plot the ARPES constant energy contours and the DFT-calculated iso-energy contours, respectively, and highlight the constant energy contours at 0.13 (Figure 4c) and 0.4 eV (Figure 4d). In both cases when approaching the massive Dirac gapped region from the Fermi level there is a clear evolution in the Fermi surface from hexagram to hexagon, that shrinks in the gapped region to a point which corresponds to the bottom of the electron band at ≈ 0.2 eV, then at 0.25 eV in

the hole band the surface texture evolves back into a hexagram upon moving further into the hole band. The overall warping away from the Massive Dirac region is reminiscent of Bi_2Te_3 .^[3] It should be noted there is some discrepancy between experiment and theory. The experimental Fermi surface shows a hexagon shape, and it overlaps well with the center part of the contour in the DFT calculations. However, the overall shape of the Fermi surface does not show the full hexagram-shape outline as predicted in the calculation. This is because as reported in Figure 3, the contribution from the bulk bands that represent the hexagram features at $k = 0.2 \text{ \AA}^{-1}$ are extremely faint and washed out by the dominant surface state bands in the ARPES iso-energy contour.

The band anisotropy in the Dirac electron band and the warping strength can be explained and modelled by adopting and modifying the Dirac Hamiltonian model of Bi_2Te_3 proposed by Fu.^[28] We include an energy gap to describe the exchange coupling of the TSS with the exchange field $\Delta_e \sigma_z$, where σ_z is the Pauli matrix from the top and bottom surface MBT SLs:

$$\varepsilon(k) = D - \sqrt{(\Delta_e + \lambda k^3 \cos(3\theta))^2 + v_F^2 k^2} \quad (1)$$

where D denotes doping level, Δ_e represents the exchange gap, λ is the warping strength, v_F the asymptotic Fermi velocity at large momenta away from the gapped region, k is the wave vector, and θ the polar angle with respect to the ΓK direction.

To examine the hexagonal warping strength, we first fit the band dispersion, blue points in Figure 3c, of the electron band

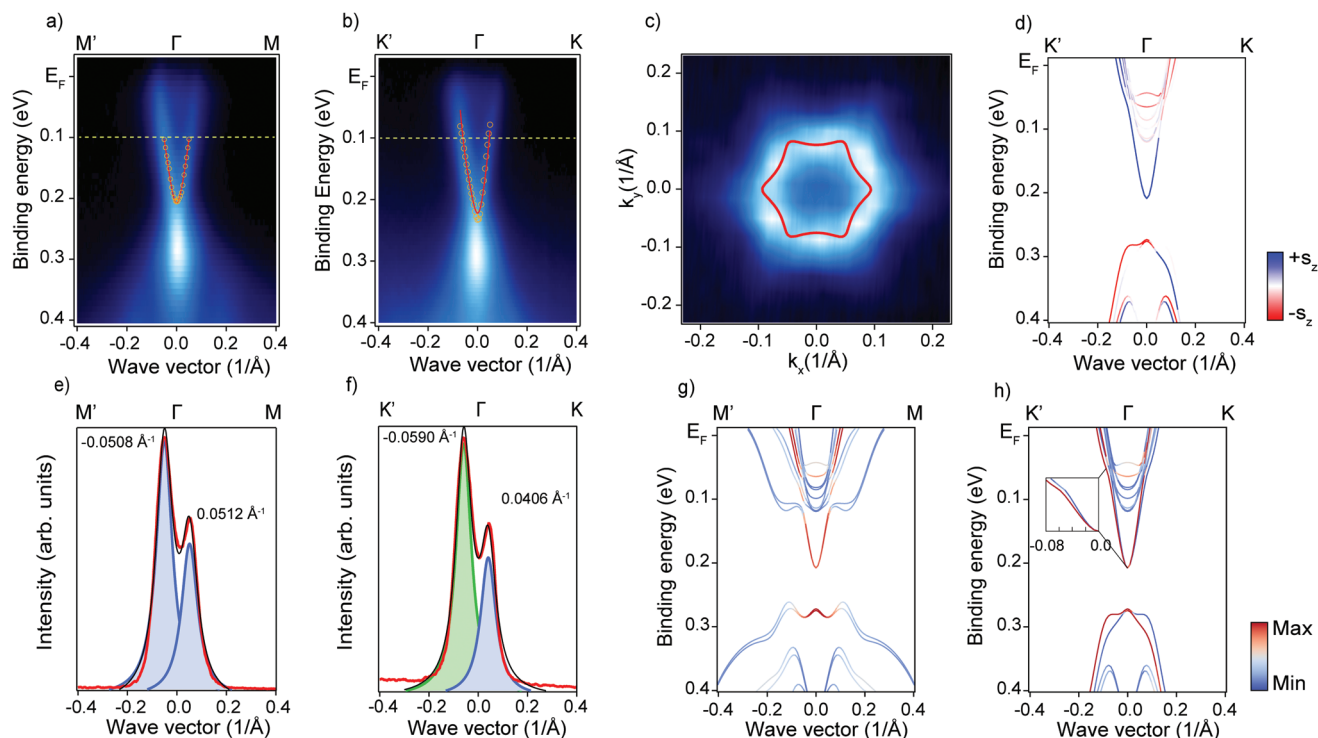


Figure 5. Demonstration of time-reversal symmetry breaking and the exchange-Rashba effect. a) ARPES spectrum taken along the $M'-\Gamma-M$ direction at 63 eV photon energy, 8 K with p-polarized light. The band is symmetric about Γ due to the preserved mirror symmetry and vanishing s_z along the ΓM direction. b) ARPES spectrum taken along $K'-\Gamma-K$ at 63 eV photon energy, 8 K with p-polarized light. c) The Fermi surface scan overlaid with the contour from the model using Equation (1). d) Spin-projected DFT. (e) and (f) represent momentum distribution curves (MDC) taken at 0.1 eV binding energy from (a) and (b) (yellow dashed line), respectively, and are fitted with two Lorentzian peaks of the same full width at half maximum. A clear asymmetry is observed for $K'-\Gamma-K$ after careful calibration of the Γ point. g, h) DFT-calculated top surface atom projected band structure along $M'-\Gamma-M$ (symmetric) and $K'-\Gamma-K$ (asymmetric), respectively.

along $\Gamma-M$ where $\lambda = 0$ to Equation (1). From the extracted EDC and MDC we perform a linear fit of the data away from the gapped region to obtain $v_F = 5.0 \pm 0.5 \times 10^5 \text{ m s}^{-1}$, which also yields a value for the doping, $D = 0.28 \text{ eV}$ that corresponds to extrapolating the linear fit to $k = 0$. Based on this v_F and D we then set Δ_e as a fitting parameter to yield $\Delta_e = 78 \text{ meV}$. This Δ_e value obtained from fitting to the gapped Dirac model is consistent with the gap value of 75 meV obtained from the EDC fitting method. By fixing Δ_e and v_F , we now fit the $\Gamma-K$ direction to determine the hexagonal warping strength, $\lambda = 418 \text{ eV \AA}^3$, which is almost twice as strong as the strength in Bi_2Te_3 ($\approx 250 \text{ eV \AA}^3$).^[28] We overlay the extracted data points from EDC peak fitting (circles) and the model (solid line) to the ARPES spectra in Figures 5a,b for $\Gamma-M$ and $\Gamma-K$, respectively, showing excellent agreement. Furthermore, we overlay our model with the Fermi surface data in Figure 5c and reproduce the key features observed experimentally.

We now proceed to confirm the magnetic origin of the bandgap in the MBT/BT/MBT heterostructure by demonstrating the observation of band asymmetry as a consequence of broken TRS known as the exchange-Rashba effect.^[29] The interplay between the hexagonal warping and magnetization in our MBT/BT/MBT heterostructure is also expected to result in a band asymmetry along the $K'-\Gamma-K$ directions. In this case, the hexagonal warping term also introduces a non-zero k -dependent out-of-plane spin texture with eigenvalue of

s_z reaching maxima at K points and zero at M points in the Brillouin zone. Because the warping term is odd under inversion, without exchange interaction, s_z at minus K point (K') is opposite to s_z at positive K, as in Bi_2Te_3 .^[28] and the band dispersion along $K'-\Gamma-K$ remains symmetric. After introducing magnetization perpendicular to the sample surface which breaks the TRS, the exchange field causes the energy shift in the surface state where the energy of states in the $\Gamma K'$ direction with spin s_z parallel to the field direction is lowered while the energy of states along ΓK is increased. As a result, the band dispersion in the surface state along the $K'-\Gamma-K$ direction is asymmetric but remains symmetric along $M'-\Gamma-M$ because of vanishing out-of-plane spin s_z . In comparison, the Dirac bands in Bi_2Te_3 thin films and bulk crystals are symmetric about Γ in the $K'-\Gamma-K$ directions.^[3,30]

We look for evidence of this in our ARPES spectrum taken at 8 K and photon energy of 63 eV along the $M'-\Gamma-M$ and $K'-\Gamma-K$ directions shown in Figures 5a,b, respectively. Without further analysis, a strong dichroism is already visible in both spectra. To probe this predicted asymmetry, we plot MDC taken at 0.1 eV below E_F for both the $M'-\Gamma-M$ and $K'-\Gamma-K$ directions in Figures 5e,f. We then fit the MDCs with two Lorentzian line shapes with identical full width at half maximum (FWHM), for $M'-\Gamma-M$ and obtain -0.0508 ± 0.01 and $+0.051 \pm 0.01 \text{ \AA}^{-1}$ corresponding to a negligible asymmetry in the Dirac electron band, consistent with the theoretical prediction that along ΓM the Dirac bands are

symmetric. The fitting for $K'-\Gamma-K$ on the other hand reveals the position of the left Dirac electron band to be $-0.059 \pm 0.01 \text{ \AA}^{-1}$ while the right branch position sits at $0.041 \pm 0.01 \text{ \AA}^{-1}$, yielding an asymmetry of 0.018 \AA^{-1} , which is greater than our angular resolution of 0.01 \AA^{-1} . We rule out this asymmetry arises from sample misalignment; details can be found in Section 11, Supporting Information. This splitting in k of 0.018 \AA^{-1} and band velocity of 3.3 eV \AA allows us to calculate an exchange field of $\approx 60 \text{ meV}$, which further corroborates our bandgap value obtained from the EDC analysis mentioned above. We also performed ARPES measurements along ΓK direction at 50 K, which is well above the Curie temperature to demonstrate the disappearance of dispersion asymmetry as shown in Figure S10, Supporting Information. At 50 K the MDCs along the $K'-\Gamma-K$ direction can only be fit with two symmetric Lorentzian line shapes corresponding to a negligible asymmetry in the Dirac electron band. The vanishing of the dispersion asymmetry is a result of restored TRS as the single-septuple layer MnBi_2Te_4 becomes paramagnetic above its Curie temperature and the exchange field becomes zero. Furthermore, the fitting also demonstrates that the peak area ratio along $K'-\Gamma-K$ is 1.8, compared with 1.7 along $M'-\Gamma-M$. The linear dichroism in the $\Gamma-K$ direction has contributions from both broken mirror symmetry from the polarized synchrotron light electric field and magnetization. In the $\Gamma-M$ direction, with out-of-plane spin s_z being almost zero, the dichroism originates largely from the light induced symmetry breaking. Therefore, the increase of 0.1 in the peak area ratio in $\Gamma-K$ can be attributed to the magnetization, that is, the exchange field couples to different s_z components in left and right branches of Dirac electron band along the $\Gamma-K$ direction as shown in Figure 5d for the s_z direction the right branch near the bandgap is flipped to the magnetization direction so that the band becomes asymmetric. These states then enter the initial state in the dipole matrix element and result in the dichroism. We then examine the DFT-calculated surface atom projected band structure in Figures 5g,h, which shows the surface states from both the top and bottom surfaces related by inversion and also predicts this dispersion asymmetry along $K'-\Gamma-K$. The blue and red bands that are symmetric about Γ represent the top and bottom surface bands that are related by spatial inversion symmetry. Since only the top surface (red) can be probed in an ARPES experiment, the bands along $K'-\Gamma-K$ will be asymmetric due to broken inversion symmetry and TRS on the top and bottom surfaces. The above discussion on dispersion asymmetry corresponding to exchange gap of 60 meV, and the ARPES measurements above the Curie temperature that show the bandgap vanishes allows us to confirm that the gap opening is primarily caused by broken TRS rather than quantum confinement.

3. Conclusion

We have grown a designer FMI/TI/FMI vdW heterostructure $[\text{MnBi}_2\text{Te}_4]_{1\text{SL}}-[\text{Bi}_2\text{Te}_3]_{4\text{QL}}-[\text{MnBi}_2\text{Te}_4]_{1\text{SL}}$, which is a robust QAH insulator with a bandgap of $75 \pm 15 \text{ meV}$. We observe the bandgap vanishes above the Curie temperature, and the exchange-Rashba effect confirms the magnetic origin of the bandgap due to broken TRS. The realization of robust bandgap in a designer heterostructure provides a crucial step towards

QAH effect and axion insulator phases at elevated temperatures. It also establishes such designer heterostructures as promising platforms for studying novel topological phases and for high-temperature lossless transport applications. Finally, these heterostructures may also be utilized for realizing recently predicted resonant photovoltaic effects^[31] that require both strong hexagonal warping and broken Kramer degeneracy.

4. Experimental Section

Thin films of MnBi_2Te_4 , Bi_2Te_3 and MBT/BT/MBT were grown using MBE on n-type doped silicon (111) substrates under ultrahigh vacuum. The samples were immediately transferred after growth to an interconnected ARPES chamber at HERS Beamline 10.0.1, Advanced Light Source (ALS), Lawrence Berkeley National Laboratory.

MnBi₂Te₄/Bi₂Te₃/MnBi₂Te₄ Thin-Film Growth on Si (111) Substrate: Effusion cells were used to evaporate elemental Bi (99.999%), Te (99.95%), and Mn (99.9%) for growth. The deposition rates were measured with a quartz crystal microbalance before growth to ensure the flux ratio of Te to Bi and Mn is greater than 10:1. The silicon (111) substrate was flash annealed to achieve the 7×7 surface reconstruction observed in RHEED. The substrate temperature was then kept at $230 \text{ }^\circ\text{C}$ during the growth process, as this temperature was determined to yield the highest quality growth based off oscillations in the RHEED intensity indicating layer-by-layer growth. 1SL MnBi_2Te_4 was achieved by first growing 1 QL of Bi_2Te_3 , then a bilayer of MnTe was deposited in order to spontaneously form MnBi_2Te_4 .^[22,32] The 1SL MnBi_2Te_4 was subsequently annealed in Te flux for 5–10 min to improve crystallinity. Following this, 4QL Bi_2Te_3 was grown, followed by 1SL MnBi_2Te_4 . The sample was then annealed in Te flux for 10 min at $230 \text{ }^\circ\text{C}$ to improve crystallinity. RHEED taken along the $[11\bar{2}]$ and $[110]$ directions are shown in Figure S1, Supporting Information. The sharp high-intensity streaks in the pattern indicate large area single crystal epitaxial growth.

Angle-Resolved Photoelectron Spectroscopy (ARPES) Measurements: Our ARPES measurements were performed at Beamline 10.0.1 with linear polarized synchrotron light and data was taken using a Scienta R4000 analyzer at temperatures between 8 and 50 K. The overall energy resolution is 15 meV. The angular resolution is 0.2° or momentum resolution $\approx 0.01 \text{ \AA}^{-1}$ for the photoelectron kinetic energies measured.

Density Functional Theory Calculations: The first-principles calculations are based on the DFT, using the projector augmented wave (PAW) method^[33] as implemented in the Vienna Ab initio Simulation Package (VASP).^[34,35] The generalized gradient approximation (GGA) with Perdew–Burke–Ernzerhof (PBE) realization^[36] were adopted for the exchange–correlation potential. The plane-wave cutoff energy was set to be 400 eV. To account for the correlation effects for Mn 3d-electrons, we used the GGA+ U method introduced by Dudarev et al.^[37] and the value of $U_{\text{eff}} = U - J$ was chosen as 5.34 eV which was adopted from the work of Otrokov et al.^[26] The vdW corrections have been taken into account by making use of the DFT-D3 approaches.^[38]

The structure models for $(\text{Bi}_2\text{Te}_3)_4$ and $(\text{MnBi}_2\text{Te}_4)/(\text{Bi}_2\text{Te}_3)_{n=4}/(\text{MnBi}_2\text{Te}_4)$ heterostructures were constructed by stacking the Bi_2Te_3 quintuple layers or MnBi_2Te_4 septuple layers in the order of ABC sequence. For the $(\text{MnBi}_2\text{Te}_4)/(\text{Bi}_2\text{Te}_3)_{n=4}/(\text{MnBi}_2\text{Te}_4)$ heterostructures, the inversion symmetry is preserved. A vacuum layer of 20 Å thickness is added to avoid artificial interactions between periodic images. The in-plane lattice parameters of these slab structures were fixed to the experimental value of Bi_2Te_3 , which is 4.3835 \AA .^[39] The Brillouin zone was sampled by the k -grid with a spacing of $2\pi \times 0.02 \text{ \AA}^{-1}$ within a Γ -centered sampling scheme for structural optimization and electronic structure calculations. Spin–orbit coupling was considered when performing the structural optimization. The energy and force convergence criteria were set to be 10^{-6} eV and $10^{-2} \text{ eV \AA}^{-1}$, respectively. The surface-resolved band structures were plotted using PyProcar.^[40] From the DFT results, we constructed the maximally localized Wannier functions (MLWFs) for Mn-d, Bi-p, and Te-p orbitals using WANNIER90.^[41–43] The iso-energy

spectrum, the edge spectrum, as well as the AHC were then calculated by means of WannierTools.^[44]

Magnetic Measurements: Magnetic measurements were performed between 4–300 K on a Quantum Design Physical Property Measurement system equipped with the vibrating sample magnetometry (VSM) module. The applied fields ranged from 0 to 20 kOe. The samples were mounted on a low background quartz holder, with the magnetic field orientated in the film plane. The diamagnetic contribution from the silicon substrate was subtracted using a fit to the high field data at 300 K.

Statistical Analysis: Data processing and analysis such as peak fitting was performed using WaveMetrics IGOR PRO software.

Supporting Information

Supporting Information is available from the Wiley Online Library or from the author.

Acknowledgements

M.T.E. was supported by ARC DECRA fellowship DE160101157. M.T.E., C.X.T., Q.L., and N.M. acknowledge funding support from ARC Centre for Future Low Energy Electronics Technologies (FLEET) CE170100039. M.T.E., Q.L., and C.X.T. acknowledge travel funding provided by the International Synchrotron Access Program (ISAP) managed by the Australian Synchrotron, part of ANSTO, and funded by the Australian Government. This research used resources of the Advanced Light Source, which is a DOE Office of Science User Facility under contract no. DE-AC02-05CH11231. S.A.Y. acknowledges funding from Singapore Ministry of Education AcRF Tier 2 (Grant MOE2019-T2-1-001). D.C. was supported by DE180100314.

Open access publishing facilitated by Monash University, as part of the Wiley - Monash University agreement via the Council of Australian University Librarians.

Conflict of Interest

The authors declare no conflict of interest.

Author Contributions

M.T.E. devised the experiments. Q.L. analyzed the data with assistance from M.T.E. Q.L. and C.X.T. performed the MBE growth at Monash University. Q.L. and C.X.T. performed the MBE growth and ARPES measurements at the ALS with the support from J.H. and S.-K.M. The DFT calculations were performed by W.W. and S.A.Y. D.C. performed the magnetometry studies. Q.L. and M.T.E. composed the manuscript. All authors read and contributed feedback to the manuscript. The authors acknowledge Michael Fuhrer for fruitful discussions.

Data Availability Statement

The data that support the findings of this study are available from the corresponding author upon reasonable request.

Keywords

heterostructure thin films, lossless transport, magnetic proximity, magnetic topological insulators, quantum anomalous Hall insulators

Received: September 20, 2021

Revised: March 3, 2022

Published online: March 31, 2022

- [1] L. Fu, C. L. Kane, E. J. Mele, *Phys. Rev. Lett.* **2007**, *98*, 106803.
- [2] M. Z. Hasan, C. L. Kane, *Rev. Mod. Phys.* **2010**, *82*, 3045.
- [3] Y. L. Chen, J. G. Analytis, J. H. Chu, Z. K. Liu, S. K. Mo, X. L. Qi, H. J. Zhang, D. H. Lu, X. Dai, Z. Fang, S. C. Zhang, I. R. Fisher, Z. Hussain, Z. X. Shen, *Science* **2009**, *325*, 178.
- [4] Y. L. Chen, J. H. Chu, J. G. Analytis, Z. K. Liu, K. Igarashi, H. H. Kuo, X. L. Qi, S. K. Mo, R. G. Moore, D. H. Lu, M. Hashimoto, T. Sasagawa, S. C. Zhang, I. R. Fisher, Z. Hussain, Z. X. Shen, *Science* **2010**, *329*, 659.
- [5] E. D. L. Rienks, S. Wimmer, J. Sánchez-Barriga, O. Caha, P. S. Mandal, J. Růžička, A. Ney, H. Steiner, V. V. Volobuev, H. Groiss, M. Albu, G. Kothleitner, J. Michalička, S. A. Khan, J. Minár, H. Ebert, G. Bauer, F. Freyse, A. Varykhalov, O. Rader, G. Springholz, *Nature* **2019**, *576*, 423.
- [6] C. Liu, Y. Wang, H. Li, Y. Wu, Y. Li, J. Li, K. He, Y. Xu, J. Zhang, Y. Wang, *Nat. Mater.* **2020**, *19*, 522.
- [7] C.-Z. Chang, J. Zhang, X. Feng, J. Shen, Z. Zhang, M. Guo, K. Li, Y. Ou, P. Wei, L.-L. Wang, Z.-Q. Ji, Y. Feng, S. Ji, X. Chen, J. Jia, X. Dai, Z. Fang, S.-C. Zhang, K. He, Y. Wang, L. Lu, X.-C. Ma, Q.-K. Xue, *Science* **2013**, *340*, 167.
- [8] C.-Z. Chang, W. Zhao, D. Y. Kim, H. Zhang, B. A. Assaf, D. Heiman, S.-C. Zhang, C. Liu, M. H. W. Chan, J. S. Moodera, *Nat. Mater.* **2015**, *14*, 473.
- [9] Q. L. He, L. Pan, A. L. Stern, E. C. Burks, X. Che, G. Yin, J. Wang, B. Lian, Q. Zhou, E. S. Choi, K. Murata, X. Kou, Z. Chen, T. Nie, Q. Shao, Y. Fan, S.-C. Zhang, K. Liu, J. Xia, K. L. Wang, *Science* **2017**, *357*, 294.
- [10] M. Mogi, R. Yoshimi, A. Tsukazaki, K. Yasuda, Y. Kozuka, K. S. Takahashi, M. Kawasaki, Y. Tokura, *Appl. Phys. Lett.* **2015**, *107*, 182401.
- [11] Y. Deng, Y. Yu, M. Z. Shi, Z. Guo, Z. Xu, J. Wang, X. H. Chen, Y. Zhang, *Science* **2020**, *367*, 895.
- [12] I. Lee, C. K. Kim, J. Lee, S. J. L. Billinge, R. Zhong, J. A. Schneeloch, T. Liu, T. Valla, J. M. Tranquada, G. Gu, J. C. S. Davis, *Proc. Natl. Acad. Sci. USA* **2015**, *112*, 1316.
- [13] S. Bhattacharyya, G. Akhgar, M. Gebert, J. Karel, M. T. Edmonds, M. S. Fuhrer, *Adv. Mater.* **2021**, *33*, 2007795.
- [14] S. K. Chong, K. B. Han, A. Nagaoka, R. Tsuchikawa, R. Liu, H. Liu, Z. V. Vardeny, D. A. Pesin, C. Lee, T. D. Sparks, V. V. Deshpande, *Nano Lett.* **2018**, *18*, 8047.
- [15] X. Yao, B. Gao, M. G. Han, D. Jain, J. Moon, J. W. Kim, Y. Zhu, S. W. Cheong, S. Oh, *Nano Lett.* **2019**, *19*, 4567.
- [16] F. Katmis, V. Lauter, F. S. Nogueira, B. A. Assaf, M. E. Jamer, P. Wei, B. Satpati, J. W. Freeland, I. Eremin, D. Heiman, P. Jarillo-Herrero, J. S. Moodera, *Nature* **2016**, *533*, 513.
- [17] R. Watanabe, R. Yoshimi, M. Kawamura, M. Mogi, A. Tsukazaki, X. Z. Yu, K. Nakajima, K. S. Takahashi, M. Kawasaki, Y. Tokura, *Appl. Phys. Lett.* **2019**, *115*, 102403.
- [18] L. Webster, J.-A. Yan, *Phys. Rev. B* **2018**, *98*, 144411.
- [19] C. Gong, L. Li, Z. Li, H. Ji, A. Stern, Y. Xia, T. Cao, W. Bao, C. Wang, Y. Wang, Z. Q. Qiu, R. J. Cava, S. G. Louie, J. Xia, X. Zhang, *Nature* **2017**, *546*, 265.
- [20] Y. Li, Z. Jiang, J. Li, S. Xu, W. Duan, *Phys. Rev. B* **2019**, *100*, 134438.
- [21] M. M. Otrokov, I. P. Rusinov, M. Blanco-Rey, M. Hoffmann, A. Y. Vyazovskaya, S. V. Eremin, A. Ernst, P. M. Echenique, A. Arnau, E. V. Chulkov, *Phys. Rev. Lett.* **2019**, *122*, 107202.
- [22] C. X. Trang, Q. Li, Y. Yin, J. Hwang, G. Akhgar, I. Di Bernardo, A. Grubišić-Čabo, A. Tadich, M. S. Fuhrer, S.-K. Mo, N. V. Medhekar, M. T. Edmonds, *ACS Nano* **2021**, *15*, 13444.
- [23] Y.-Y. Li, G. Wang, X.-G. Zhu, M.-H. Liu, C. Ye, X. Chen, Y.-Y. Wang, K. He, L.-L. Wang, X.-C. Ma, H.-J. Zhang, X. Dai, Z. Fang, X.-C. Xie, Y. Liu, X.-L. Qi, J.-F. Jia, S.-C. Zhang, Q.-K. Xue, *Adv. Mater.* **2010**, *22*, 4002.
- [24] Y. Hou, J. Kim, R. Wu, *Sci. Adv.* **2019**, *5*, eaaw1874.

- [25] T. Hirahara, S. V. Ereemeev, T. Shirasawa, Y. Okuyama, T. Kubo, R. Nakanishi, R. Akiyama, A. Takayama, T. Hajiri, S.-i. Ideta, M. Matsunami, K. Sumida, K. Miyamoto, Y. Takagi, K. Tanaka, T. Okuda, T. Yokoyama, S.-i. Kimura, S. Hasegawa, E. V. Chulkov, *Nano Lett.* **2017**, *17*, 3493.
- [26] M. M. Otrokov, T. V. Menshchikova, M. G. Vergniory, I. P. Rusinov, A. Yu Vyazovskaya, Y. M. Koroteev, G. Bihlmayer, A. Ernst, P. M. Echenique, A. Arnau, E. V. Chulkov, *2D Mater.* **2017**, *4*, 025082.
- [27] O. V. Yazyev, J. E. Moore, S. G. Louie, *Phys. Rev. Lett.* **2010**, *105*, 266806.
- [28] L. Fu, *Phys. Rev. Lett.* **2009**, *103*, 266801.
- [29] M. M. Otrokov, I. I. Klimovskikh, H. Bentmann, D. Estyunin, A. Zeugner, Z. S. Aliev, S. Gaß, A. U. B. Wolter, A. V. Koroleva, A. M. Shikin, M. Blanco-Rey, M. Hoffmann, I. P. Rusinov, A. Y. Vyazovskaya, S. V. Ereemeev, Y. M. Koroteev, V. M. Kuznetsov, F. Freyse, J. Sánchez-Barriga, I. R. Amiraslanov, M. B. Babanly, N. T. Mamedov, N. A. Abdullayev, V. N. Zverev, A. Alfonsov, V. Kataev, B. Büchner, E. F. Schwier, S. Kumar, A. Kimura, et al, *Nature* **2019**, *576*, 416.
- [30] G. Wang, X.-G. Zhu, Y.-Y. Sun, Y.-Y. Li, T. Zhang, J. Wen, X. Chen, K. He, L.-L. Wang, X.-C. Ma, J.-F. Jia, S. B. Zhang, Q.-K. Xue, *Adv. Mater.* **2011**, *23*, 2929.
- [31] P. Bhalla, A. H. MacDonald, D. Culcer, *Phys. Rev. Lett.* **2020**, *124*, 087402.
- [32] Y. Gong, J. Guo, J. Li, K. Zhu, M. Liao, X. Liu, Q. Zhang, L. Gu, L. Tang, X. Feng, D. Zhang, W. Li, C. Song, L. Wang, P. Yu, X. Chen, Y. Wang, H. Yao, W. Duan, Y. Xu, S.-C. Zhang, X. Ma, Q.-K. Xue, K. He, *Chin. Phys. Lett.* **2019**, *36*, 089901.
- [33] P. E. Blöchl, *Phys. Rev. B* **1994**, *50*, 17953.
- [34] G. Kresse, J. Hafner, *Phys. Rev. B* **1994**, *49*, 14251.
- [35] G. Kresse, J. Furthmüller, *Phys. Rev. B* **1996**, *54*, 11169.
- [36] J. P. Perdew, K. Burke, M. Ernzerhof, *Phys. Rev. Lett.* **1996**, *77*, 3865.
- [37] S. L. Dudarev, G. A. Botton, S. Y. Savrasov, C. J. Humphreys, A. P. Sutton, *Phys. Rev. B* **1998**, *57*, 1505.
- [38] S. Grimme, J. Antony, S. Ehrlich, H. Krieg, *J. Chem. Phys.* **2010**, *132*, 154104.
- [39] M. H. Francombe, *Br. J. Appl. Phys.* **1958**, *9*, 415.
- [40] U. Herath, P. Tavadze, X. He, E. Bousquet, S. Singh, F. Muñoz, A. H. Romero, *Comput. Phys. Commun.* **2020**, *251*, 107080.
- [41] N. Marzari, D. Vanderbilt, *Phys. Rev. B* **1997**, *56*, 12847.
- [42] I. Souza, N. Marzari, D. Vanderbilt, *Phys. Rev. B* **2001**, *65*, 035109.
- [43] A. A. Mostofi, J. R. Yates, Y.-S. Lee, I. Souza, D. Vanderbilt, N. Marzari, *Comput. Phys. Commun.* **2008**, *178*, 685.
- [44] Q. Wu, S. Zhang, H.-F. Song, M. Troyer, A. A. Soluyanov, *Comput. Phys. Commun.* **2018**, *224*, 405.